PHYSICAL REVIEW FLUIDS **4**, 054704 (2019)

Active control of vortex shedding from a blunt trailing edge using oscillating piezoelectric flaps

Bradley Gibeau, Charles Robert Koch, and Sina Ghaemi[*]
Department of Mechanical Engineering, University of Alberta, Edmonton, Alberta T6G 2R3, Canada

(Received 12 November 2018; published 28 May 2019)

Piezoelectric bending actuators have been used to drive flaps to manipulate vortex shedding from a nominally two-dimensional blunt trailing edge (BTE) using three different actuation methods. The experiments were conducted in a wind tunnel at a Reynolds number of $\mathrm{Re}(h) = 2600$ where h is the height of the BTE. A combination of base-pressure measurements at the BTE and high-speed particle image velocimetry was used to characterize actuator performance over their operating range. Proper orthogonal decomposition was also applied to study the energy content of the primary vortex shedding structures in the wake during actuation. Cases of significant vortex shedding amplification and suppression were investigated. Vortex shedding amplification occurred when the frequency of actuation matched that of the natural wake process, resulting in the turbulent kinetic energy associated with two-dimensional vortex shedding increasing from 70% to 90%. This led to higher turbulence intensities, a shortened recirculation region, and more organized vortex shedding in general. Vortex shedding suppression was caused by the generation of small spanwise vortices at the tips of the actuators, which disrupted the interaction between the separating shear layers. The energy associated with vortex shedding was reduced from 70% to 20% in this case, resulting in a significant attenuation of the shedding pattern for at least six BTE thicknesses downstream. Vortex shedding suppression was accompanied by greatly reduced turbulence intensities, a narrowed wake, and a lengthened recirculation region. The actuators were also capable of forcing symmetry in the near-wake using a symmetric actuation method, but the vortex shedding resumed downstream, although with a reduced frequency. Finally, an adaptive slope-seeking controller was designed using the base-pressure measurements at the BTE in real time. The closed-loop controller was capable of seeking and maintaining an optimal input for vortex shedding suppression, even during slow variations in freestream velocity.

DOI: 10.1103/PhysRevFluids.4.054704

I. INTRODUCTION

Control of vortex shedding has the potential to lead to improved bluff body aerodynamics for a variety of applications including road, marine, and aerospace vehicles. Choi *et al.* [1] characterized bluff body flow strategies into three primary groups. In order of increasing complexity, these are passive, active open-loop, and active closed-loop control strategies. Passive control refers to actuation without power input, for example, the use of geometric modifications. Active open-loop strategies utilize powered actuation, and active closed-loop control strategies utilize real-time measurements along with powered actuators so that actuation can be tailored towards a desired control outcome or operating condition. Control theory based on linear systems provides a plethora of tools for

---

[*] ghaemi@ualberta.ca

analyzing and implementing closed-loop control methods [2]; however, modeling a fluid-dynamical system and designing a controller for flow control purposes is not straightforward [3].

The successful implementation of active flow control strategies, even in a laboratory environment, is challenging. One of these challenges is selecting appropriate actuators [4], since the complex nature of fluid flows makes predicting the effects of actuation difficult. Moreover, actuators must often be implemented in a manner that is minimally invasive with respect to the overall geometry of the system so that desirable flow characteristics can be preserved. The importance of realistic actuators for flow control is emphasized in the present work, and experimental investigations are the focus of the following discussion.

During early investigations into vortex shedding control, the wakes of cylinders were actuated by means of transverse oscillations [5–7], loudspeakers [8–10], and cylinder rotation [11]. While these studies provide great insight into the mechanisms behind controlling unsteady wakes, it is often impractical to rely on moving the entire body itself or generating acoustic noise to control flow. The use of steady injection or suction[12,13], synthetic jets [12,14–18], plasma actuators [19–25], and control cylinders [26,27] has become popular more recently for use with various bluff body geometries. Aside from the latter, these types of actuators can be implemented into the surface of a body to manipulate the flow while retaining the overall geometry, making them more suitable for practical applications. Despite the large variety of actuators that have been utilized during experiments, ideal actuators for flow control still elude researchers [4].

The use of piezoelectric materials to create actuators for flow control purposes is a promising area of active research [28–30]. Piezoelectric materials expand or contract when a voltage is applied and can be used to manipulate flow boundaries using various signals. They have been used to actuate the exit of a square jet [31,32], generate vortices in a boundary layer [33–36], attenuate cavity oscillations [37], and manipulate separation on an airfoil [38,39]. More closely related to the present investigation, they have also been used to suppress and enhance vortex shedding from both elastically and rigidly mounted square cylinders [40,41]. In these studies, the actuator was mounted under a plastic plate on the top surface of the cylinder and acted to perturb the surface upwards during actuation to enhance and reduce the effects of vortex shedding on the square cylinder by tuning a proportional-integral-derivative (PID) controller. Zhang *et al.* [40,41] were able to alter the effects associated with vortex shedding, namely, enhanced and reduced vortex circulation, velocity fluctuations, lift forces, and drag forces. Although they concluded that the enhancement and suppression of vortex shedding was due to whether the actuator motion was in- or out-of-phase with the transverse fluid motion, their investigation lacked a detailed analysis of the mechanism responsible for vortex shedding enhancement and suppression. The use and potential of piezoelectric actuators for wake control is therefore still an open research question.

There are generally three potential outcomes when actuation is successfully applied to an unsteady, two-dimensional wake. These are amplification, suppression, and reorganization of the classic von Kármán pattern. Amplification and suppression occur when the natural vortex shedding process is strengthened or weakened, respectively. In the case of amplification, the von Kármán pattern is retained, but the strength of the shed vortices is enhanced. Wake reorganization occurs when the structure of the von Kármán wake pattern is altered in some way, resulting in a different spatial organization of the spanwise wake vortices. All three of these cases will be detailed next.

Amplification of the unsteadiness in the wake often occurs through resonant forcing leading to the occurrence of a "lock-in" scenario. The classical case of lock-in is the resonant vibration of a flexibly-mounted cylinder when vortices shed from the trailing edge during cross-flow [42]. This classical case is due to self-excitation, but forcing transverse oscillations can also lead to amplification of the vortex shedding pattern [6,7]. Vortex shedding amplification has been achieved recently using two of the more promising types of flow control actuators: plasma actuators [20,22] and synthetic jets [16]. The results of these studies indicate that amplified vortex shedding is generally accompanied by increases in turbulence intensities in the wake, pressure drag, and force fluctuations on the body. As well, Benard and Moreau [22] reported vortices that shed closer to the body, resulting in a more organized shedding pattern and a shorter recirculation region.

Suppression of the unsteady wake is a commonly sought control outcome. Many of the previously discussed investigations were able to achieve vortex shedding suppression to some degree, resulting in attenuation of the unwanted pressure variations in the wake. Interestingly, vortex shedding suppression does not always occur through the same mechanisms. The slot synthetic jets used by Pastoor *et al.* [16] attenuated vortex shedding in the wake by forcing the symmetric (simultaneous) roll-up of the two shear layers at the trailing edge of the body, leading to the postponement of shedding to farther downstream and an increase in base pressure by 40%. The slot synthetic jet used by Fujisawa *et al.* [15] generated small spanwise vortices in one shear layer which weakened the interaction between the separating shear layers, leading to disruption of the wake pattern and complete attenuation of lift fluctuations on the body. Although the actuators used were similar, different mechanisms (forced symmetry versus shear layer disruption) were responsible for wake suppression, thus highlighting the importance of studying these mechanisms.

An interesting result of actuation is the potential spatial reorganization of the vortex structures in the wake. This occurs in the wakes of cylinders when the cylinder is vibrated in a specific manner, and the results include various symmetric and asymmetric vortex patterns [42–44]. The reorganization of the wake to a symmetric mode is interesting from an engineering perspective because it results in the removal of mean and fluctuating lift forces on the body which normally occur due to cyclic wake asymmetry caused by vortex shedding. Moreover, it has been shown that forcing the symmetric mode can lead to delayed vortex shedding and an increase in base pressure as previously discussed [16]. In this regard, forced wake symmetry (and other reorganization patterns) has the potential to be considered a suppression of vortex shedding. The symmetric shedding mode has mostly been observed in the wake of an oscillating cylinder but has also been forced using sound [45], freestream flow oscillations [46,47], and the aforementioned synthetic jets [16,17].

Considering the literature reviewed here, it is evident that many types of flow control actuators can be used to manipulate vortex shedding. However, the versatility of piezoelectric actuators for wake control has not been fully explored. This type of actuator has many unique benefits. For example, they can be made into various shapes, can be flush-mounted into a surface, and can take a wide range of input signals and convert them into a user-defined displacement pattern. The present investigation studies the use of piezoelectric bending actuators for manipulating vortex shedding from a blunt trailing edge (BTE). The bending actuator used is a multilayered cantilever beam whose free end is displaced during actuation. Several of these actuators are used to drive flaps in an oscillatory manner, and the resulting effect on the wake over their entire operating range is characterized for three different actuation methods: symmetric, asymmetric, and single actuation. Base-pressure measurements at the BTE are used to determine how the actuation influences the frequency content in the near-wake. The results are used to select cases of interest for further study using high-speed particle image velocimetry (PIV). Proper orthogonal decomposition (POD) is applied to the PIV data to determine the turbulent kinetic energy content in the wake that is attributable to vortex shedding during actuation, and cases of vortex shedding amplification, suppression, and reorganization are addressed. Finally, an adaptive slope-seeking control strategy is applied to optimize the actuation frequency in real time for the purpose of vortex shedding suppression.

II. EXPERIMENTAL SETUP

The trailing edge of a nominally two-dimensional blunt model has been modified for control purposes and studied in a wind tunnel. Pressure fluctuation measurements and high-speed PIV were utilized to study the wake with and without active control being applied. The experiments were conducted at a Reynolds number of $\mathrm{Re}(h) = 2600$ where h is the height of the BTE. The boundary layer upstream from the BTE is laminar under these conditions, as was demonstrated in a previous study using the same two-dimensional blunt model [48].

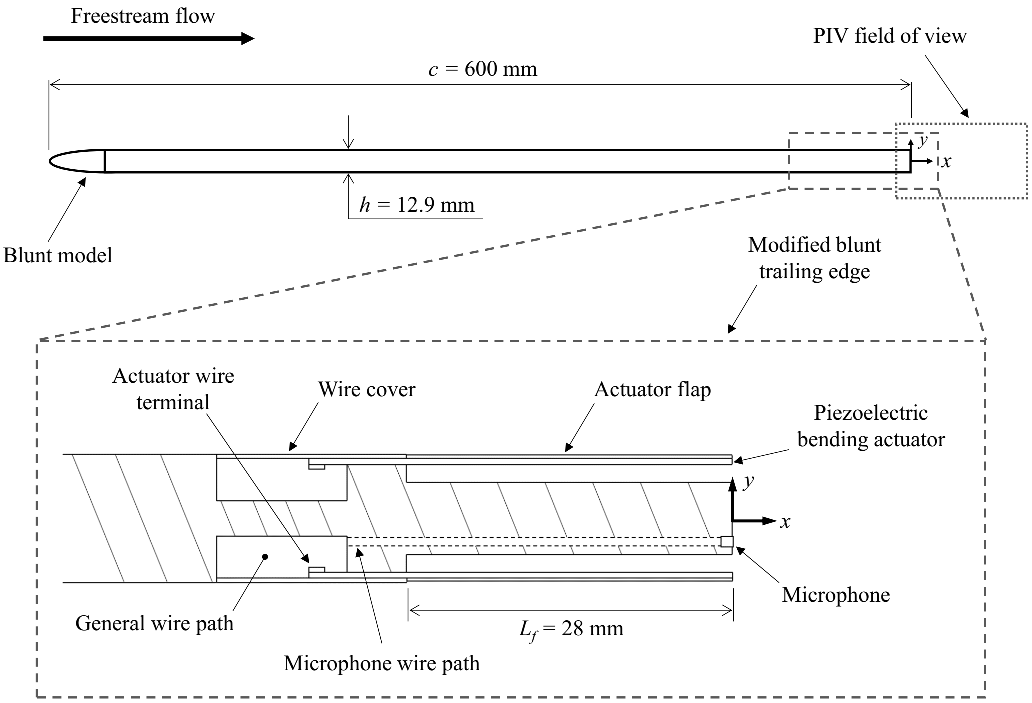

FIG. 1. Schematic of the experiment and sectional view of the modified BTE. Note that the z coordinate runs in the spanwise direction with $z = 0$ located at center span.

A. Wind tunnel facility and blunt model

The wind tunnel used for the experiments is a closed-loop facility that is capable of flow speeds up to 35 m/s. The test section is surrounded by glass or acrylic windows on all four sides for PIV, and the cross-sectional dimensions are 2.4×1.2 m^2 ($W \times H$). Honeycombs, several screens, and a 6.3:1 contraction are used to condition the flow, resulting in turbulence intensities of less than 0.4% when the flow speeds are greater than 2 m/s [49].

A flat aluminum plate with a fine surface finish was used to create the blunt model. The leading edge of the plate was made semielliptical to prevent upstream flow separation, and the chord length was cut to $c = 600$ mm. The model was oriented vertically at zero angle of attack during experiments and spanned the entire height of the test section. The height of the BTE was $h = 12.9$ mm, resulting in a negligible blockage of 0.5% within the wind tunnel.

The BTE has been modified for control as depicted in Fig. 1. Note that the spanwise direction is denoted by z, and $z = 0$ is center span. Both sides of the BTE feature cantilevered flaps that are used to interact with the flow. They are made of 0.005-inch (0.127-mm) stainless-steel sheets that span 10 cm in the z direction and when not actuated are flush-mounted with the surface of the blunt model. The inner surface of each flap is adhered to five piezoelectric bending actuators (PI Ceramic, PICMA PL128.10), and each actuator has dimensions of $36 \times 6.3 \times 0.75$ mm^3 ($L \times W \times T$). The manufacturer reports a resonant frequency of 360 Hz and a maximum tip displacement of 0.9 mm. Each set of five actuators acts in unison to displace the free end of one flap, and the free length of each actuator-flap construction is $L_f = 28$ mm. A relatively short span of the BTE is actuated, but it has been shown that control of vortex shedding within a small spanwise cell is possible because the flow in adjacent cells is uncorrelated [9]. Two 1/8-inch (3.2-mm) microphones (Knowles, FG-23629-P16) have been installed to measure the fluctuation in pressure at the BTE as is shown in the zoomed-in view within Fig. 1. The microphones are placed at $z = \pm 1$ cm in the spanwise direction and are offset towards one side of the trailing edge so that the phase of the nearest shear layer can be monitored if desired (e.g., Pastoor *et al.* [16]). An I/O board (dSPACE, 1103) has been utilized along with Simulink (MATLAB) and Control Desk (dSPACE) to realize real-time implementation of the actuators and microphones. All microphone signals have been sampled at a rate of 500 Hz, corresponding to roughly 10× the natural vortex shedding frequency for the investigated Re.

B. High-speed particle image velocimetry

Two-component, high-speed PIV has been conducted to evaluate the impact of the actuators on the wake flow. A dual-cavity Nd:YLF laser (Photonics Industries, DM20-527-DH) was used with a combination of spherical and cylindrical lenses to produce a laser sheet at center span ($z = 0$) with a thickness of 2 mm. Each cavity of the laser emits light at 527 nm with a pulse width of 170 ns. The pulses from both cavities can be combined to produce 40 mJ per pulse at 1 kHz or can be used in an alternating fashion to obtain frequencies up to 20 kHz with lower power. A high-speed camera (Phantom, v611) featuring a 1280 × 800-pixel CMOS sensor ($20 \times 20\ \mu\text{m}^2$ pixel size, 12-bit resolution) was used to collect time-resolved images. A Nikon lens with a focal length of $f = 200$ mm and an aperture setting of $f/4$ was applied to obtain a field of view (FOV) of $(\Delta x, \Delta y) = 91 \times 57\ \text{mm}^2$ $(7.0h \times 4.4h)$ with a digital resolution of $70.8\ \mu\text{m/pix}$. Sets of 5400 single-frame images were collected at a frequency of 5 kHz [$\text{St}(h) = 20$] for the unforced wake and for numerous actuation cases. The FOV used for PIV is visible in Fig. 1.

The collected images were processed using DaVis 8.2 software (LaVision GmbH). The minimum of the collected ensembles was subtracted to reduce background noise, and the resulting images were divided by ensemble averages for normalization. The preprocessed images were cross-correlated using a multipass algorithm that utilized 48 × 48 pixel (3.40 × 3.40 mm) interrogation windows with 75% overlap for the final pass. Two successive images were correlated to obtain each vector field, resulting in 5399 vector fields per collected ensemble. No postprocessing was applied to these vector fields.

C. Actuator dynamics and actuation methods

The piezoelectric flaps are resonant devices, i.e., they are limited by their own resonant frequency. It is necessary to determine this frequency for the actuator-flap combination to avoid actuating in a potentially self-destructive manner during resonance. This has been done by imaging the displacement of the flap using the same high-speed camera that was used for PIV. The same lens with an extension ring was employed to obtain an improved resolution of $22.4\ \mu\text{m/pix}$. The system was then used to collect time-resolved images of the piezoelectric flap tip displacement (d_{tip}) as a function of actuation frequency (f_a). The actuators were driven by a zero-mean sinusoid with the maximum actuation voltage of $V_a = \pm 30$ V for this analysis. The resulting frequency response is given in Fig. 2, where it is evident that the resonant frequency of the piezoelectric flap is approximately 215 Hz. This is below the manufacturer-reported resonant frequency of each actuator (360 Hz) because the stainless-steel flaps add mass to each system of five actuators. The maximum frequency used to drive the piezoelectric flaps in all subsequent tests is $f_{\max} = 180$ Hz [$\text{St}(h) = 0.73$]. This corresponds to a maximum tip displacement of 0.9 mm, and therefore all actuation is submillimeter.

The protrusion of the flap into the freestream is half that of the total tip displacement because the actuators bend symmetrically about their resting positions. This is at most 0.45 mm given the maximum tip displacement. When considering the thickness of the BTE (12.9 mm), the maximum protrusion into the freestream flow during actuation is less than 3.5% of the BTE height. The blockage by the actuators is therefore assumed to be negligible and is expected to have a negligible impact the pressure drag acting on the body as a result of geometric changes alone.

A simple analysis can be conducted to determine whether the pressure variations in the flow affect the actuator dynamics. The maximum pressure variation is assumed to occur between the

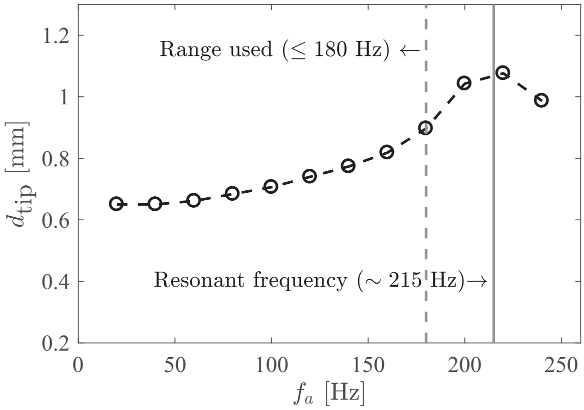

FIG. 2. Frequency response of the piezoelectric flap construction. The tip displacement (d_{tip}) was measured using a calibrated high-speed camera with a resolution of 22.4 μm/pix, and the piezoelectric flap was driven using a sinusoid of maximum amplitude (±30 V).

freestream and stagnation, which corresponds to a pressure change of 6 Pa at the Re considered here. The actuator manufacturer reports a force output of 0.5 N per actuator. Given that five actuators drive each flap, this is a total force output of 2.5 N. Considering the dimensions of each flap (100×28 mm^2), the pressure caused by the flap during actuation is estimated to be 893 Pa. The maximum pressure variations caused by the flow are therefore more than an order of magnitude weaker than the pressure output of the flaps, and the effect of the flow field on the actuator dynamics is negligible.

Three different open-loop actuation methods have been explored in this work. These are symmetric, asymmetric, and single actuation and have been named for their movement with respect to the wake center line (the x axis in Fig. 1). Schematic representations of all three actuation methods are given in Fig. 3. Actuation has been generated using a zero-mean sinusoid for all cases moving forward, and only the amplitude and frequency were modified. The five piezoelectric actuators driving one flap received the same input voltage signal. Sending the same signal to the row of actuators on the second flap results in symmetric actuation. The second signal was either phase shifted by π radians or removed altogether to obtain asymmetric or single actuation, respectively.

D. Base-pressure measurements

The signals from the two microphones located at $z = \pm 1$ cm were averaged to obtain a measure of base pressure fluctuation at center span, denoted as P'. The power spectral density (PSD) of P' has been determined for the unforced wake at $\text{Re}(h) = 2600$ to obtain the unforced vortex shedding frequency. This value is $f_u = 49.5$ Hz and corresponds to a Strouhal number of $\text{St}(h) = 0.20$. This

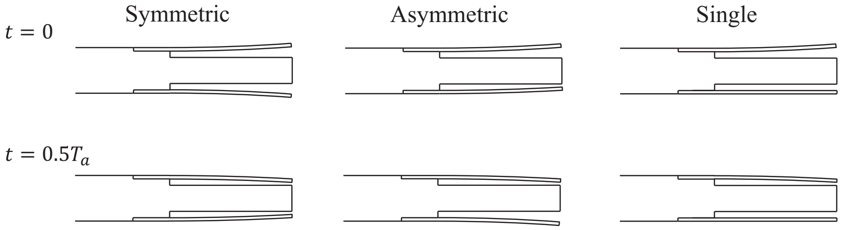

FIG. 3. Schematic representation of the symmetric, asymmetric, and single actuation methods. Note that T_a is the period of actuation.

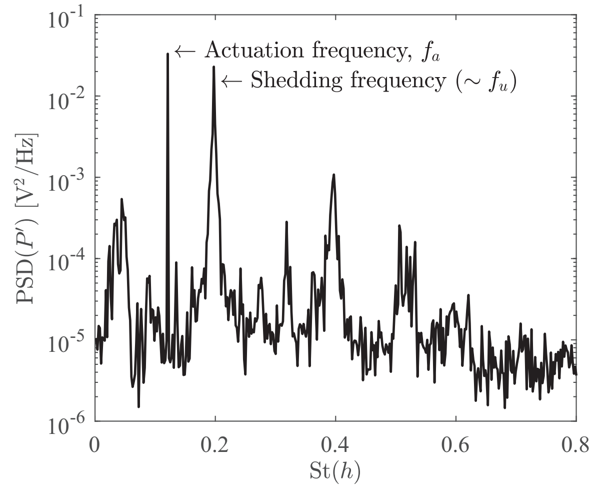

FIG. 4. Power spectral density (PSD) of P' at Re(h) = 2600 for symmetric actuation at 30 Hz. The plot indicates that the pressure fluctuations caused by vortex shedding and the acoustic actuation noise are the only significant contributors to the microphone signal.

St is similar to the values reported in the wake of circular cylinders [50], and slightly smaller than other reported values in the wake of a BTE [51].

The actuators produce acoustic noise at their driving frequency which contaminates the microphone measurement of hydrodynamic pressure fluctuation. Despite this, it is possible to monitor the frequency content of the vortex shedding using PSD if the actuation frequency is known and is different than the shedding frequency. This is evident when looking at the sample PSD of P' in Fig. 4, where clear peaks exist for both the vortex shedding frequency ($\sim f_u$) and the actuation frequency ($f_a = 30$ Hz). The plot also reveals that the pressure fluctuations in the wake caused by vortex shedding and the acoustic noise produced by the actuators are the only sources with a significant contribution to the microphone signal. The unsteady wake can be said to be suppressed if the peak corresponding to vortex shedding is no longer present in the spectrum.

The strength of vortex shedding in the near-wake as measured by the microphones can be monitored using a suppression variable (σ) defined as

$$\sigma = 10 \log \left(\frac{S_a}{S_u} \right), \tag{1}$$

where S (subscripts for actuated and unforced cases) denotes the sum of the energy associated with vortex shedding according to the peak in the PSD associated with the vortex shedding frequency. The values for S have been determined by integrating PSD(P') over a small window w surrounding the peak in the spectrum:

$$S = \int_w \mathrm{PSD}(P')\, df. \tag{2}$$

The window w had a width of 8 Hz and was centered on f_u for the present analysis. Note that a value of $\sigma = 0$ dB represents zero suppression of the unsteady wake, and that the suppression variable cannot be evaluated when $f_a = f_u$ due to overlap of the peaks.

E. Adaptive slope-seeking control

Adaptive slope seeking allows for a system to seek optimal control inputs in real time if a measurement of the plant to be controlled is available [52]. The method has been applied

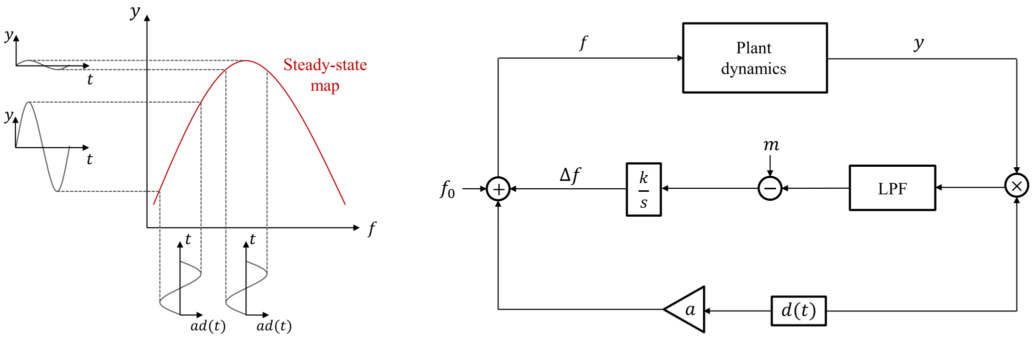

FIG. 5. Left: Schematic representation of how the dither signal $ad(t)$ provides a measure of the slope of the steady-state map, which is proportional to the magnitude of the output oscillations; schematic adapted from Becker *et al.* [55]. Right: The control loop structure implemented here for adaptive slope seeking.

in numerous flow control experiments, often in the context of extremum seeking. Successful experimental implementations include controlling backwards-facing step flows [53,54], airfoil separation [55–58], cavity oscillations [59], jet mixing [60], and unsteady wakes [16,61]. A properly designed slope-seeking controller is able to guide the output of a system to a specified location on a steady-state input-output map by seeking a reference slope. A slope of zero is sought when the control goal is to drive the output to an extremum on the steady-state map. A small nonzero slope is used as the reference when the map features a plateau. A brief overview of adaptive slope seeking is given below, and the reader is referred to Ariyur and Krstić [52] for a rigorous overview of the standard slope-seeking method.

A vital component of the slope-seeking method is the use of a dither signal. The dither signal takes the form of a zero-mean waveform (usually a sinusoid) and is added to the system input to perturb the system in a regular manner. As long as the system is operating at a position on the steady-state map with a nonzero slope, this oscillating component to the input will cause the output to oscillate in a similar manner. When the system reaches an extremum, the oscillations in the output are minimized due to the shape of the steady-state map. The slope of the steady-state map is therefore monitored by measuring the degree to which the output oscillates with respect to the dither signal, and this is shown schematically in Fig. 5. The frequency and amplitude of the dither signal must be selected appropriately to ensure that the output of the plant oscillates along with the dither signal, i.e., the dither must be slow enough to allow for the plant dynamics to reach steady state during each dither cycle, and the amplitude must be large enough to elicit a response from the system. Adaptive slope seeking does not stabilize unstable plant dynamics, but instead, it acts to guide the output of the system to an optimal point on the steady-state map of a stable plant.

The control loop structure used for the current application of adaptive slope seeking is presented in Fig. 5. The input to the system f is the sum of the initial input f_0, the control modification Δf, and the dither signal $ad(t)$. The measured system output is denoted as y. The control structure is modified compared to the standard slope-seeking loop and is based off the work of Brackston *et al.* [61]. The major modification to the standard slope-seeking loop is the removal of the high-pass filter, which becomes redundant with a properly designed low-pass filter. Specifically, a moving-average filter with a period of $2\pi/\omega_d$ is selected, where $\omega_d = 2\pi f_d$ is the frequency of the dither signal in radians. This filter results in complete attenuation of the harmonics of ω_d, which remain unaccounted for if the high-pass filter is removed. A second modification to the standard control loop is the use of a square wave dither signal as opposed to a sinusoid. This change is made because the input to the system is the frequency of actuation in the present investigation. The result would be an actuator driving frequency that is itself changing in a sinusoidal manner, resulting in unwanted broadband frequency content [61]. Thus, the square wave dither is used here, and the control input

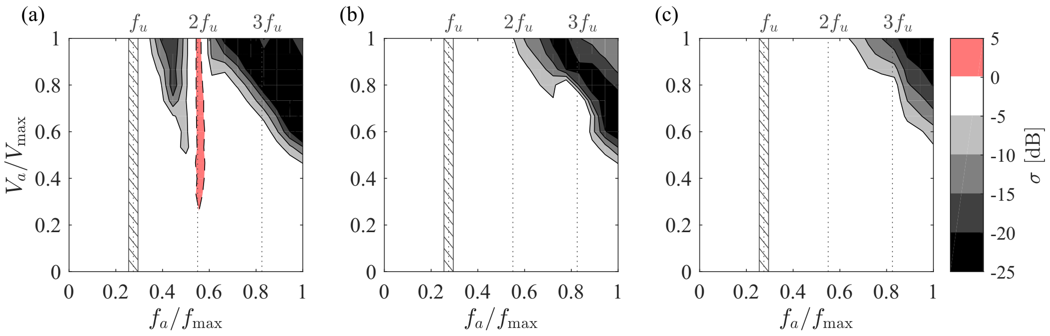

FIG. 6. Contour plots of the suppression variable [σ; see Eq. (1)] over the entire operating envelope for (a) symmetric, (b) asymmetric, and (c) single actuation. Solid lines denote negative contours, and dashed lines denote positive contours. The hatched section centered at f_u represents an area of no data, as σ cannot be evaluated near the unforced wake frequency. Note that $V_{\max} = 30$ V and $f_{\max} = 180$ Hz.

is updated only when the square wave changes from 1 to -1 or vice versa. The signal driving the actuators during adaptive slope seeking is therefore a sinusoid of constant amplitude whose frequency changes in a stepwise manner. The other components of the control loop structure in Fig. 5 include the reference slope m and the integrator k/s.

III. RESULTS AND DISCUSSION

A. Actuation envelopes

The suppression variable (σ) presented in Eq. 1 is used here to evaluate the performance of the actuators over their entire operating range for symmetric, asymmetric, and single actuation. The actuator driving frequencies have been varied from 10 to 180 Hz in increments of 10 Hz, and the amplitudes have been varied from 2 to 30 V in increments of 2 V, resulting in 270 data points for each method. Each value of σ has been determined using 10 sec of microphone data, corresponding to roughly 500 unforced wake cycles. The results have been formed into the contour plots of Fig. 6, where the upper horizontal axis displays actuation frequencies normalized by the unforced wake frequency ($f_u = 49.5$ Hz) and the hatched section represents a region where σ cannot be evaluated due to contamination by acoustic noise from the actuators (see Sec. II D). It is interesting to note that all three actuation methods appear to be able to suppress vortex shedding in the wake at high actuation amplitudes and frequencies as is evident in the upper right corner of each plot. This suggests that there is a threshold phenomenon at play, and this threshold appears to be above $f_a = 2f_u$ for all cases. Moreover, symmetric actuation [Fig. 6(a)] results in behavior that is not present for asymmetric and single actuation. This includes vortex shedding amplification at $f_a = 2f_u$ and a second region of vortex shedding suppression that occurs within $1 < f_a/f_u < 2$.

These contour plots have led to the selection of six cases of interest for each actuation method. These are actuation at $f_a/f_u = 1.0$, 1.5, 2.0, 2.5, 3.0, and 3.5 at the maximum actuation amplitude ($V_a/V_{\max} = 1$) for all three actuation methods, thus covering all potential regions of vortex shedding suppression and amplification. High-speed PIV of the wake (described in Sec. II B) has been conducted for all 18 cases of interest as well as for the unforced wake to study the response of the vortex shedding to actuation. These data ensembles will be the focus of the analysis for the next four subsections.

B. Analysis of wake energy

The POD of streamwise velocity by the method of snapshots [62] has been applied to all PIV data ensembles. This has been done to study the interaction between actuation and the primary instability.

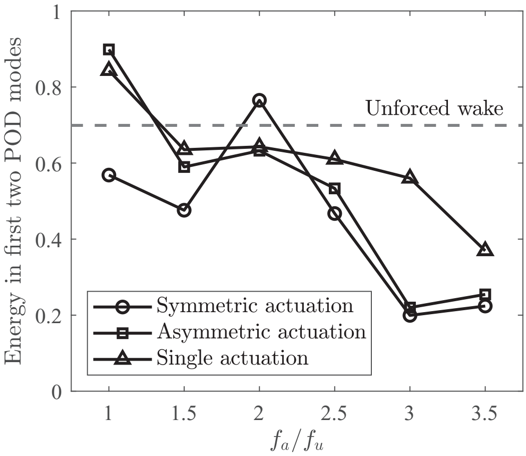

FIG. 7. Energy content within the first two POD modes used to identify the strength of the primary vortex shedding instability. Maximum vortex shedding suppression occurs at $f_a = 3f_u$ for symmetric and asymmetric actuation and at $f_a = 3.5f_u$ for single actuation. Cases of vortex shedding amplification are visible at $f_a = f_u$ and $2f_u$.

With respect to a periodic wake, it is known that the first two POD modes represent the dynamics of two-dimensional vortex shedding and contain a large fraction of the fluctuation energy in the wake flow [63]. These two modes are used here to monitor the coherence of the vortex shedding pattern during actuation.

The energy contained within the first two modes of the unforced wake represents approximately 70% of the wake fluctuation energy, and the third mode contains only 2.4%. This demonstrates that the unforced wake is dominated by the primary vortex shedding instability. The total energy captured by the first two POD modes is plotted in Fig. 7 as a function of actuation frequency for the 18 selected cases. The trends in Fig. 7 agree with those determined using the microphone signals in Fig. 6. Specifically, significant vortex shedding suppression occurs beyond $f_a = 2f_u$ for all cases. Once again, symmetric actuation reveals amplification at $f_a = 2f_u$ and a second suppression region located in the range $1 < f_a/f_u < 2$. Two more cases of vortex shedding amplification are visible, corresponding to asymmetric and single actuation at $f_a = f_u$ (the region in Fig. 6 where σ could not be evaluated due to signal contamination by acoustic noise from the actuators), and this is likely due to resonant forcing between the actuation cycles and the primary instability. The most effective vortex shedding amplification occurs during asymmetric actuation at $f_a = f_u$, resulting in a vortex shedding pattern that contains 90% of the fluctuation energy in the flow. Conversely, symmetric actuation at $f_a = 3f_u$ leads to the maximum suppression of the vortex shedding pattern, resulting in the first two POD modes containing only 20% of the fluctuation energy. Although the first two modes contain only 20% of the fluctuation energy, what remains of the suppressed vortex shedding pattern remains low-order (see Appendix A).

When comparing Figs. 6 and 7, the POD results show that maximum suppression does not occur until $f_a = 3f_u$ for symmetric and asymmetric actuation, whereas the microphone results show this occurring closer to $f_a = 2.5f_u$ at the same actuation amplitude ($V_a = V_{\max}$). This discrepancy has been caused by the fact that the microphones are only capable of measuring the near-wake, while POD was applied to PIV data extending as far as six BTE thicknesses downstream and therefore could account for delayed wake unsteadiness. This reduced observability of the wake is a result of using flush-mounted sensors embedded into the BTE as opposed to sensors that can measure the downstream state of the wake to a greater extent.

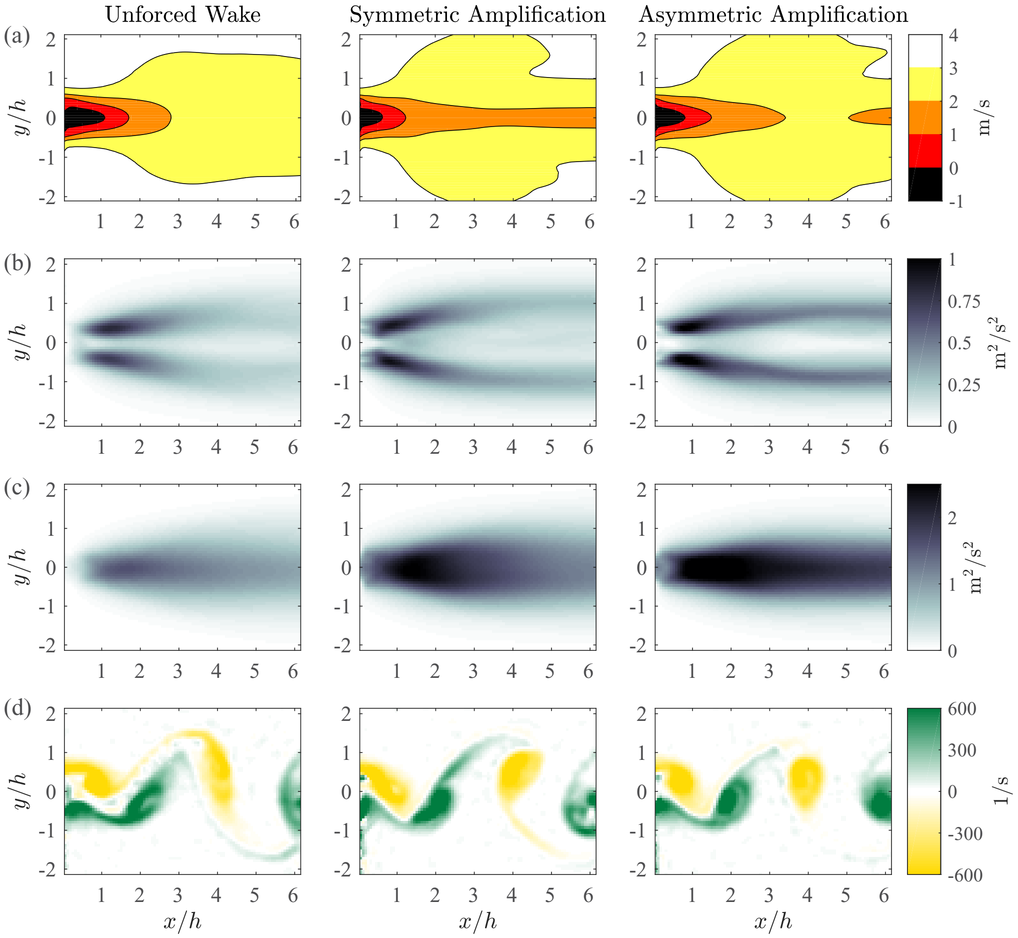

FIG. 8. (a) Mean streamwise velocity contours $\langle U \rangle$, (b) streamwise turbulence intensities $\langle u^2 \rangle$, (c) transverse turbulence intensities $\langle v^2 \rangle$, and (d) instantaneous snapshots of vorticity ω_z for the unforced and amplified wakes. Time-resolved videos of the structures in panel (d) are available in Movie 1 [65].

C. Vortex shedding amplification

Two specific instances of vortex shedding amplification will be considered here: symmetric actuation at $f_a = 2f_u$ and asymmetric actuation at $f_a = f_u$. These two cases result in an increase in the energy associated with two-dimensional vortex shedding by 7% and 20%, respectively, according to the POD analysis presented in Fig. 7. Amplification by single actuation at $f_a = f_u$ is a weaker version of the amplification caused by asymmetric actuation and is therefore not considered.

As previously discussed, vortex shedding amplification generally leads to an increase in turbulence intensities in the wake and a decrease in base pressure. The latter is related to formation length, i.e., the size of the mean recirculation region [64]. These items are investigated within Fig. 8 in comparison with the unforced wake case, where contours of mean streamwise velocity ($\langle U \rangle$), turbulence intensities ($\langle u^2 \rangle$, $\langle v^2 \rangle$), and instantaneous contours of vorticity (ω_z) are given. Note that the recirculation region is defined by $\langle U \rangle = 0$ and is therefore represented by the black region in each subplot of $\langle U \rangle$. Time-resolved measurements of ω_z are also provided in Movie 1 [65] for the natural wake and for both cases of vortex shedding amplification.

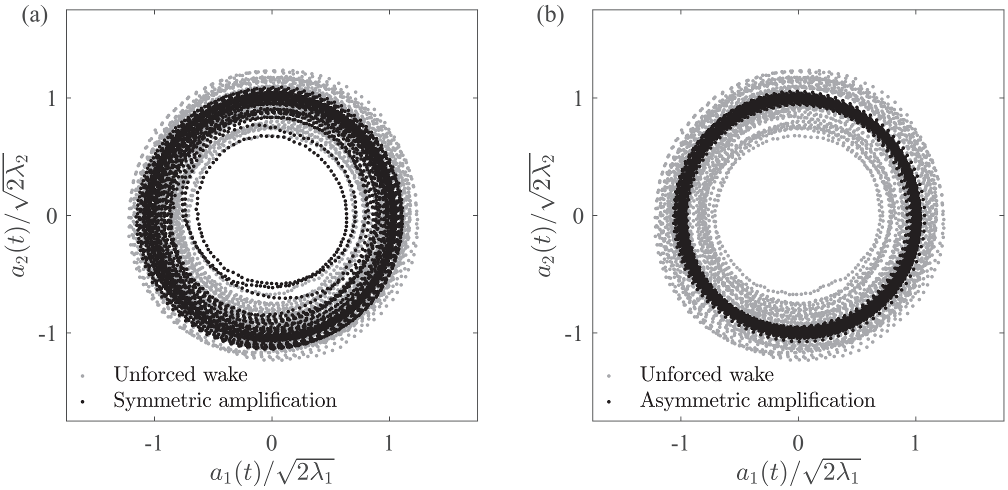

FIG. 9. Phase plots of the first two POD mode amplitudes ($a_i(t)$) normalized by the corresponding eigenvalues (λ_i) and compared to those of the unforced flow for (a) symmetric and (b) asymmetric amplification. A normalized phase plot that more closely resembles the unit circle is indicative of more coherent vortex shedding.

The mean contours of streamwise velocity presented in Fig. 8(a) show a widening of the wake and a shortening of the recirculation region for both actuation cases. Interestingly, symmetric amplification results in the shortest recirculation region, even though asymmetric amplification appears to be more effective at enhancing the primary wake instability according to Fig. 7. The shortened recirculation regions can result in a decrease in base pressure because the low-pressure cores of the shed vortices are closer to the base of the BTE. This also suggests an increase in drag for both cases. The turbulence intensities in the streamwise (x) and transverse (y) directions are investigated in Figs. 8(b) and 8(c). Both cases of vortex shedding amplification result in higher levels of turbulent fluctuations on average, with asymmetric amplification producing the largest increase. Specifically, the maximum turbulence intensity in the transverse direction doubles under asymmetric amplification, and this can be seen in Fig. 8(c). This is indicative of large velocity fluctuations in the direction normal to the freestream flow, which will increase the fluctuating forces acting on the body. Finally, the instantaneous snapshots of vorticity presented in Fig. 8(d) and the time-resolved measurements in Movie 1 [65] reveal that the amplified wakes generally lead to a more organized von Kármán pattern. The improved coherence of the shed vortices in Fig. 8(d) is clearly visible when comparing the vortices located at $x/h = 4$ within each snapshot. This is most pronounced for asymmetric amplification, which results in shed vortices that are more round and coherent compared to those of the unforced wake. These results are consistent with those of Benard and Moreau [22], who found that vortex shedding amplification through plasma actuation resulted in more organized shedding and a shortened recirculation region. They also found that the vortices shed closer to the trailing edge of the body, and this seems to be the case in the present investigation as well as is evident from the reduced recirculation regions.

The improved coherence of the shed vortices has been further investigated statistically using the results of the POD analysis. This is done using phase plots of the normalized POD coefficients from the first two modes [63]. The ideal case of two-dimensional vortex shedding will produce a phase plot corresponding to the unit circle. Any deviations from the circle can be considered to be due to amplitude and phase jitter between the various shedding cycles, i.e., larger deviations are caused by inconsistent vortex shedding. The POD mode amplitudes $a_i(t)$ for the first two modes have been normalized by the corresponding eigenvalues λ_i and are plotted against each other in Fig. 9. The

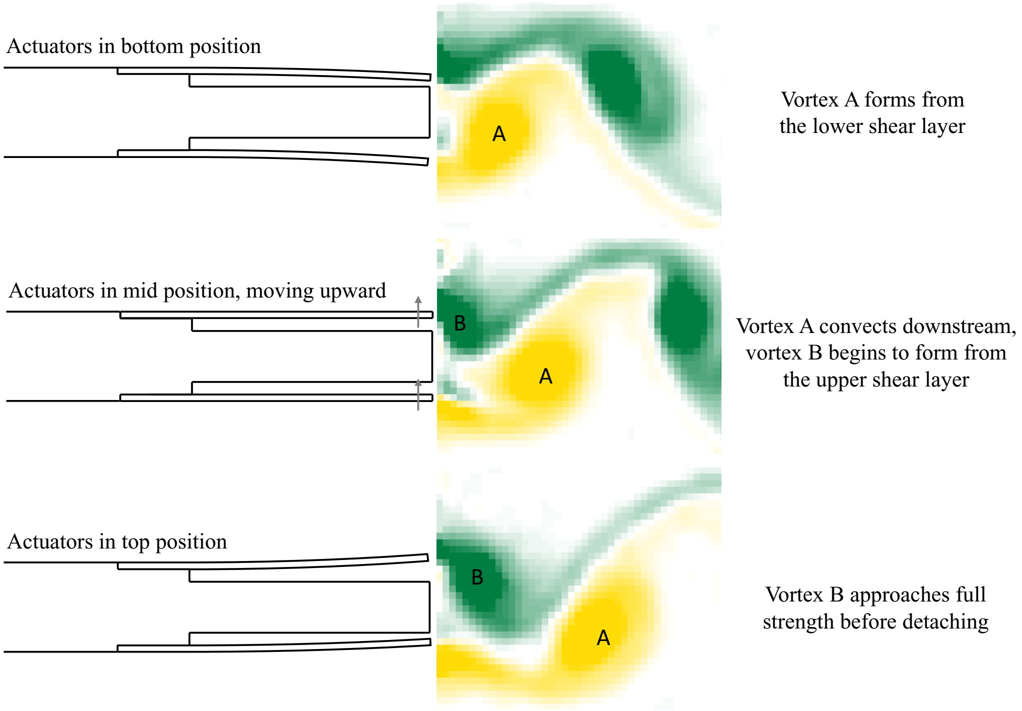

FIG. 10. Schematic of the development of the near-wake vortices relative to the piezoelectric flap movement during asymmetric vortex shedding amplification.

plots reveal that both instances of vortex shedding amplification result in more coherent vortex shedding; however, the effect is significantly more pronounced under asymmetric amplification. The lack of deviation from the tightly grouped phase circle in Fig. 9(b) is evidence of vortex lock-in during asymmetric actuation, which acts to force a more organized vortex shedding. The same evidence is not present for symmetric actuation, as the phase plot shows deviation even beyond that of the unforced wake for a short period. These results are in agreement with the instantaneous vorticity plots in Fig. 8(d) and the time-resolved measurements in Movie 1 [65], which show improved vortex shedding coherence, especially in the case of asymmetric amplification. Note that the contours of the suppression variable in Fig. 6 and the energy trends of the first two POD modes in Fig. 7 suggest that vortex shedding amplification is possible only within a narrow frequency range around $2f_u$ for symmetric actuation and f_u for asymmetric and single actuation.

Further inspection of the high-speed PIV data reveals that the mechanism behind vortex shedding amplification through asymmetric actuation is lock-in between the natural wake tendencies and the actuation cycles. The amplification process is shown in Fig. 10, where the development of the near-wake vortices is shown relative to the piezoelectric flap movement. During each actuation-shedding cycle, the piezoelectric flaps move towards the shear layer that is rolling into the near-wake to form a new spanwise vortex. The flap movement coincides with the motion of the fluid that is forming the vortex, effectively increasing the strength of that vortex until it is shed from the body. As the shear layer from the opposite corner of the BTE begins to roll into the wake, the piezoelectric flap changes directions and the cycle of vortex enhancement continues. The asymmetric motion of the piezoelectric flaps simulates transverse oscillations of a flexible trailing edge in a localized manner. This actuation is analogous to the transverse oscillation of a cylinder, which can also lead to vortex shedding enhancement through lock-in [6,7]. It should be noted that amplification through single actuation assists the forming vortex using only one piezoelectric flap, explaining why the

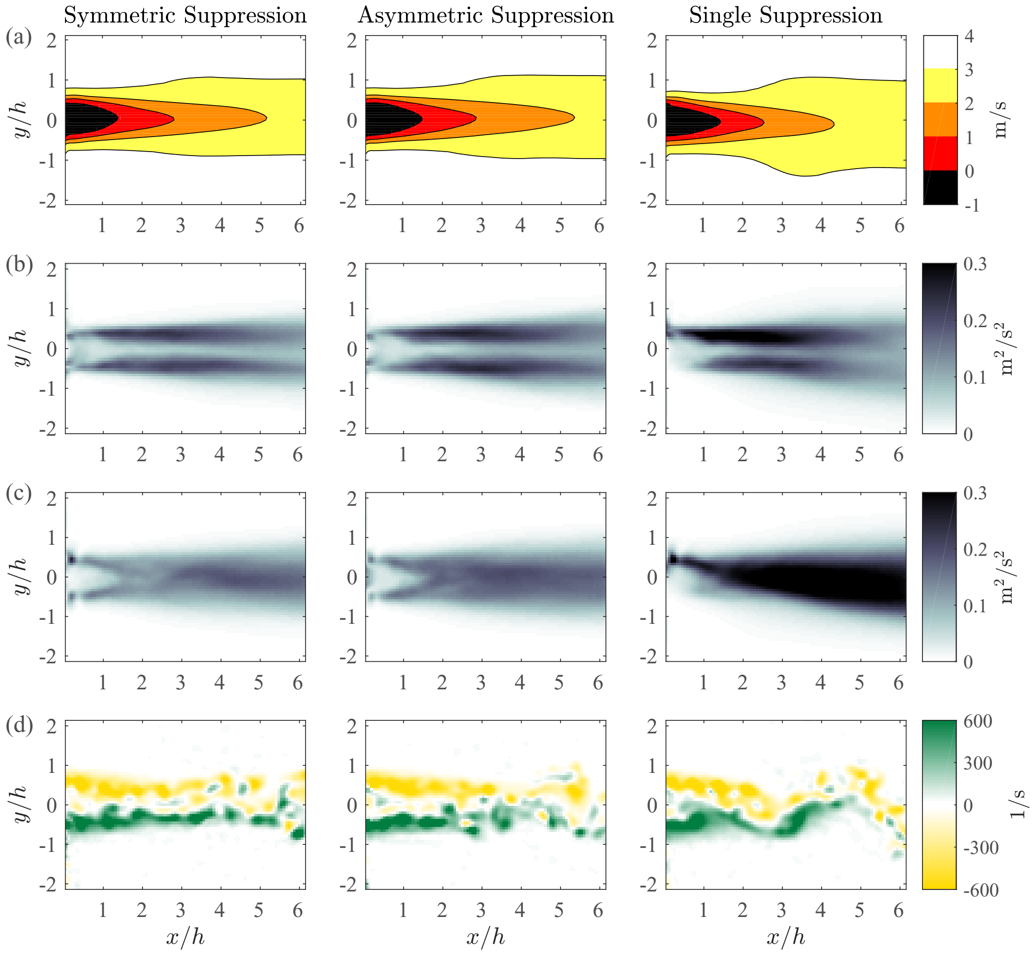

FIG. 11. (a) Mean streamwise velocity contours $\langle U\rangle$, (b) streamwise turbulence intensities $\langle u^2\rangle$, (c) transverse turbulence intensities $\langle v^2\rangle$, and (d) instantaneous snapshots of vorticity ω_z for the symmetric, asymmetric, and single actuation suppression cases. Time-resolved videos of the structures in panel (d) are available in Movie 2 [65].

amplification is reduced. Vortex shedding amplification by symmetric actuation is also similar, but one piezoelectric flap is working against the vortex strengthening process. This is likely the reason why symmetric actuation results in the weakest amplification of the wake unsteadiness.

D. Vortex shedding suppression

Suppression of the unsteady wake has been studied using the best performing actuation frequencies according to Fig. 7. This corresponds to symmetric and asymmetric actuation at $f_a = 3f_u$ and single actuation at $f_a = 3.5f_u$, resulting in the first two POD modes containing 20%, 22%, and 37% of the total fluctuation energy, respectively. This value is 70% for the unforced wake. Similarly to vortex shedding amplification, the performance of the suppression methods is first evaluated using the contours of mean streamwise velocity, turbulence intensities, and instantaneous snapshots of vorticity presented in Fig. 11, and time-resolved measurements of vorticity are provided in Movie 2 [65]. Note that the unforced wake measurements in Fig. 8 and Movie 1 [65] will be used as the reference for evaluation of the suppression cases.

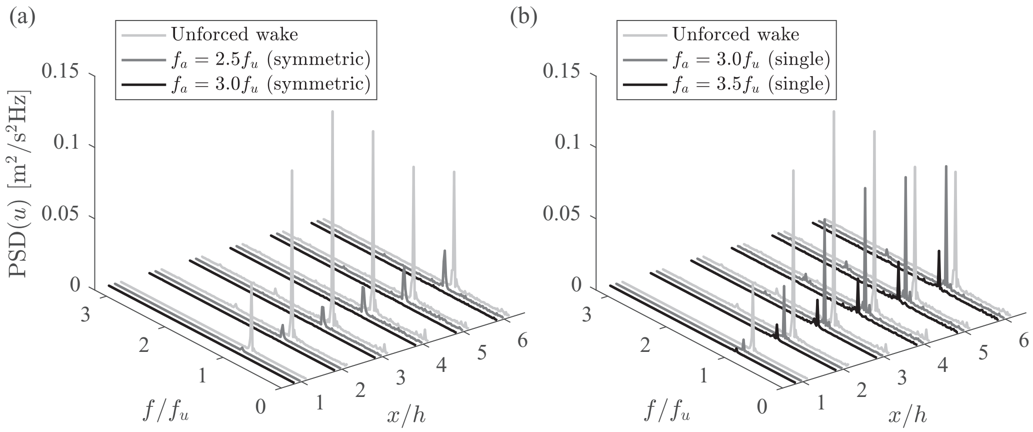

FIG. 12. Power spectral density (PSD) of the fluctuating component of streamwise velocity (u) as a function of distance from the BTE (evaluated at $y = h$) for the unforced wake and for (a) symmetric and (b) single actuation. Complete removal of the vortex shedding frequency occurs as far as $x = 6h$ downstream during symmetric actuation at $f_a = 3f_u$.

In contrast to vortex shedding amplification, the mean velocity contours in Fig. 11(a) reveal a narrowing of the wake and moderate lengthening of the recirculation region when vortex shedding is suppressed. This suggests an increase in base pressure and therefore a decrease in bluff body drag. The patterns of turbulent fluctuations have been elongated, and the magnitudes have been greatly reduced [note that the color-bar scales in Figs. 11(b) and 11(c) are significantly reduced when compared to the unforced wake reference in Figs. 8(b) and 8(c)]. Symmetric and asymmetric actuation show similar results; however, single actuation leads to less turbulence reduction and an asymmetric wake pattern. The turbulent fluctuations begin just past the tip of the piezoelectric flap before they increase and expand downstream, although they still do not reach the levels of turbulence that are present in the unforced wake.

The instantaneous vorticity plots in Fig. 11(d) and the time-resolved measurements in Movie 2 [65] reveal a complete removal of the unsteady wake pattern for symmetric and asymmetric actuation and a large reduction in the pattern for single actuation. Further inspection of these plots and the time-resolved movies reveals that the separating shear layers become populated with small concentrations of vorticity. Spanwise vortices form at the tip of the piezoelectric flaps when the flap moves away from the wake center line. The flap protruding into the high-shear flow forces this roll-up locally and results in the formation of small spanwise vortices at the frequency of actuation. These vortices disrupt the natural interaction between the separating shear layers, thus resulting in suppression of the primary instability. Similar results have been obtained by Fujisawa *et al.* [15], who found that suppression of the wake occurs when a slot synthetic jet caused the formation of small spanwise vortices directly into one of the shear layers separating from a circular cylinder. Nati *et al.* [23] also reported vortex shedding suppression via shear layer disruption, but using plasma actuators near a BTE that acted to break up the shear layers in a less-organized manner.

The frequency content in the wake has been investigated to determine whether the dominant vortex shedding frequency is still present during vortex shedding suppression. The streamwise velocity fluctuations at $y = h$ from the time-resolved PIV have been used to calculate the PSD in the wake as a function of distance from the BTE, and the results are shown in Fig. 12. Note that asymmetric actuation has been omitted from this analysis because there is a negligible difference between symmetric and asymmetric suppression. As expected, the PSD of the unforced wake contains a significant peak corresponding to the natural vortex shedding frequency. This peak is maximized at the location $x = 3h$, and there is a small frequency component present at

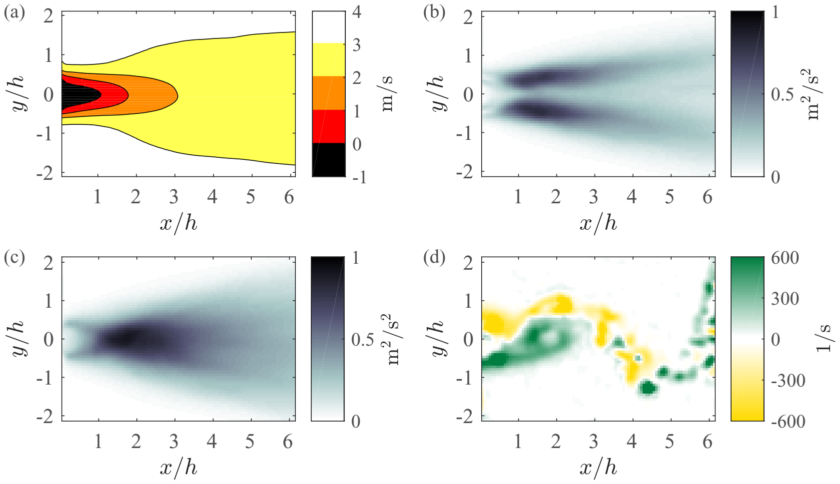

FIG. 13. (a) Mean streamwise velocity contours $\langle U \rangle$, (b) streamwise turbulence intensities $\langle u^2 \rangle$, (c) transverse turbulence intensities $\langle v^2 \rangle$, and (d) instantaneous snapshots of vorticity ω_z for symmetric actuation at $f_a = 1.5 f_u$. Time-resolved videos of the structures in panel (d) are available in Movie 3 [65].

$f = 2f_u$ that likely represents a harmonic of the natural wake. Looking at symmetric actuation in Fig. 12(a), it is evident that the maximum suppression case ($f_a = 3f_u$) completely removes the peak corresponding to the unforced vortex shedding frequency up to at least $x = 6h$ downstream. Actuation at $f_a = 2.5f_u$ greatly reduces the magnitude of the peak, but some influence of the primary instability remains, and it increases with downstream distance. Single actuation, shown in Fig. 12(b), is not able to completely suppress the frequency component corresponding to vortex shedding, but suppression increases significantly when the actuation frequency is increased from $f_a = 3f_u$ to $3.5f_u$. This is evidence that single actuation at a higher frequency than what is investigated here may result in complete suppression of the unsteady wake, suggesting that disruption of one shear layer may be sufficient for complete removal of vortex shedding. The spectra in Fig. 12 agree with the time-resolved measurements shown in Movie 2 [65], i.e., there is no clear vortex shedding pattern in the wake during symmetric and asymmetric actuation at $f_a = 3f_u$, but there is some consistent weak shedding further downstream during single actuation at $f_a = 3.5f_u$. It should also be noted that, although vortex shedding is suppressed as far as $6h$ from the BTE during maximum suppression, the primary instability and therefore wake unsteadiness have the potential to resume further downstream, although much weaker. This may be sufficient in the context of wake control, as delaying the vortex shedding process to further downstream has been shown to reduce the negative effects acting on a BTE [16].

E. Symmetric wake reorganization

The suppression region in the range $1 \leqslant f_a/f_u \leqslant 2$ for symmetric actuation visible in Figs. 6 and 7 is interesting due to its low-frequency actuation and has not yet been addressed. This region is peculiar because it occurs only for symmetric actuation and for a narrow range of frequencies. It has been further studied here using the high-speed PIV data corresponding to symmetric actuation at $f_a = 1.5f_u$. Contours of mean streamwise velocity, turbulence intensities, and instantaneous snapshots of vorticity are presented in Fig. 13, and time-resolved measurements of vorticity are provided in Movie 3 [65] with a comparison to the unforced wake case. The unforced wake plots from Fig. 8 will once again serve as the reference for Fig. 13. The figure reveals that the mean recirculation region is not significantly affected, but the overall shape of the wake changes to resemble a V. This is also true for the turbulence intensities, which are slightly higher when

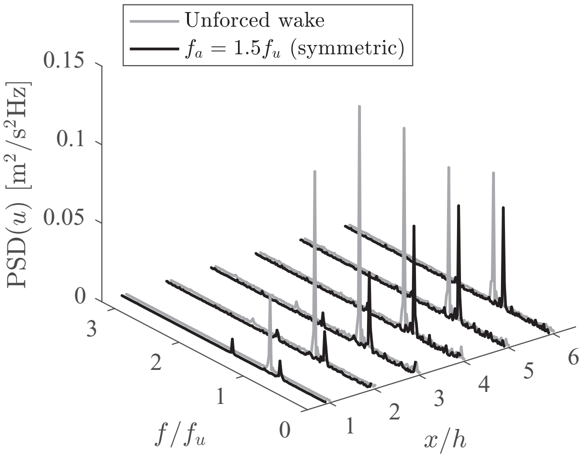

FIG. 14. Power spectral density (PSD) of the fluctuating component of streamwise velocity (u) as a function of distance from the BTE (evaluated at $y = h$) for the unforced wake and for symmetric actuation at $f_a = 1.5f_u$. The dominant wake frequency shifts to a value of $0.75f_u$ during actuation.

compared to the unforced wake. Most notably, the vorticity plot reveals that the instantaneous structure of the wake is different when compared to the previously studied cases. First, the shear layers appear to be rolling up at the BTE simultaneously, suggesting that the symmetric wake mode is being forced in the near-wake by the symmetric actuation. Second, the overall structure of the alternating vortex shedding pattern appears to be present further downstream from the BTE, but without the presence of large, coherent spanwise vortices. It appears that the symmetric mode is forced, but the natural wake tendencies begin to dominate almost immediately.

The complex interaction between the symmetric near-wake and the downstream vortex shedding is investigated using Fig. 14, which shows the PSD of u as a function of distance from the BTE for symmetric actuation at $f_a = 1.5f_u$. The plot reveals a clear shift in the dominant wake frequency to a value of approximately $0.75f_u$. This frequency is almost nonexistent in the very near-wake ($x = h$) and grows in strength with downstream distance. A small frequency component is also visible at $x = h$ corresponding to $1.5f_u$. This peak does not seem to be caused by a harmonic because it is the same magnitude as the only other peak at that streamwise location. Instead, it is likely due to the cyclic formation of the symmetric vortices caused by actuation, and its contribution to PSD is negligible at all downstream points. This suggests that the wake is still dominated by the downstream vortex shedding, despite it being delayed by the forced symmetry in the near-wake.

The source of the shift in the dominant wake frequency visible in Fig. 14 has been investigated using the time-resolved measurements in Movie 3 [65]. The movie reveals that actuation causes the two shear layers to roll into the near-wake simultaneously, but the symmetric pair of counter-rotating vortices quickly destabilizes. Each vortex pair rotates and moves to one side of the wake or the other in an alternating fashion following a typical shedding pattern before decomposing into smaller concentrations of vorticity as the pair convects downstream. However, since the vortex pairs are formed at the actuation frequency ($f_a = 1.5f_u$), and it takes two pairs to form a single shedding cycle, the shedding frequency in the wake shifts to $0.75f_u$. A schematic of the instantaneous wake structure resulting from this process is shown in Fig. 15.

Further inspection of the high-speed PIV data reveals that the symmetric wake is forced in the same way that the small spanwise vortices are generated during vortex shedding suppression, i.e., the vortices form from the shear layers when the piezoelectric flaps move away from the wake center line. The primary difference is that the actuation frequency applied here is much closer to the natural frequency of the wake. The vortices grow and interact instead of simply remaining embedded

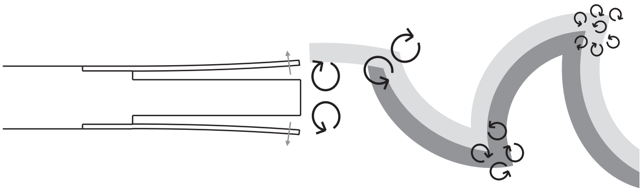

FIG. 15. Schematic of the instantaneous wake structure resulting from symmetric actuation at $f_a = 1.5 f_u$. Actuation forces the simultaneous roll-up of shear layers at the trailing edge. The resulting symmetric vortex pair quickly destabilizes and moves to one side of the wake or the other in an alternating fashion to form a shedding pattern at a reduced frequency of $0.75 f_u$. The vortex pairs break into smaller concentrations of vorticity as they convect downstream.

in the shear layers, and this is likely because the primary wake instability has more influence at this frequency. The formation of symmetric but unstable vortices during wake actuation has also been reported by Nishihara *et al.* [66], Konstantinidis and Balabani [47], and Pastoor *et al.* [16].

F. Application of adaptive slope-seeking control

The present actuation strategies allow for effective manipulation of the wake structures to achieve both amplification and suppression of vortex shedding from a BTE by varying the frequency of actuation. The results can be used to implement an adaptive slope-seeking controller to automatically seek optimal actuation frequencies in real time if a measurement of the plant to be controlled is available [52]. Here “optimal” refers to an input that locates the output of the plant at the optimal position on the steady-state map. This method of closed-loop control is applied following Sec. II E to seek optimal actuation frequencies for vortex shedding suppression using the microphone measurements at the BTE to demonstrate that the current actuator-microphone system can be used for closed-loop control purposes. A typical feedback controller, such as a PID controller, was not considered for this purpose because of the nature of the interaction between actuation and sensing. The present actuators suppress vortex shedding by generating small spanwise vortices in the wake, and it requires time for these vortices to form and interfere with the natural interaction of the shear layers. This imposes a delay between actuation and when the microphones measure the effect of actuation. This delay is too large for traditional feedback control using PID control, which requires that the timescales of the plant dynamics, actuation, and sensing be similar. The adaptive controller works on a timescale that is much larger than that of the plant dynamics and was therefore ideal for demonstrating closed-loop control using the present system of actuators and sensors.

The microphone signals were investigated in Sec. III A using the suppression variable, but calculating PSD at high rates is not straightforward. To avoid real-time spectral analysis, a band-pass filter is applied to the measurements of P' to isolate the vortex shedding signal while attenuating the acoustic noise generated by the piezoelectric flaps to allow for monitoring of the vortex shedding pattern. An implication is that actuation cannot be applied at frequencies within the pass band of the filter. This is acceptable because the wake is suppressed here at actuation frequencies that are more than twice that of the unforced wake. The band-pass-filtered microphone signal will be denoted as P'', and the root-mean-square (rms) of P'' is used to obtain a measure of the magnitude of the vortex shedding. The control objective is to minimize P''_{rms} using the actuation frequency of the piezoelectric flaps.

An advantage of closed-loop control is the ability to reject disturbances. Here the disturbance is a change in freestream velocity, which would lead to a variation in the unforced wake frequency. A small range of Reynolds numbers is considered for testing the ability of the controller to adapt to an unknown change in freestream velocity. The range considered is $2600 \leqslant \mathrm{Re}(h) \leqslant 3500$ with vortex shedding frequencies of $49.5\ \mathrm{Hz} \leqslant f_u \leqslant 68.7\ \mathrm{Hz}$. The lower and upper cutoff frequencies of

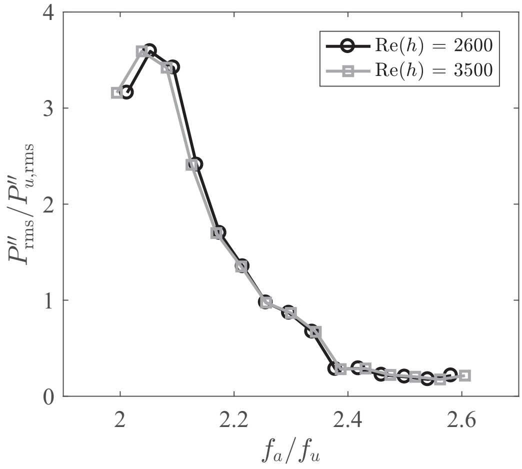

FIG. 16. The plateau-style steady-state maps for the current application of adaptive slope seeking. The optimal actuation frequency according to these maps is $f_a/f_u = 2.4$, and the map appears static within $2600 \leqslant \mathrm{Re}(h) \leqslant 3500$.

the band-pass filter have therefore been chosen to be 45 and 75 Hz to allow for the monitoring of vortex shedding using P'' within the given range.

Symmetric actuation at the maximum amplitude has been selected for closed-loop control because it results in the most effective suppression while having the smallest chance of imposing unnecessary fluctuating forces on the BTE. The actuation parameter that will be varied using slope seeking is the frequency of actuation f_a. The steady-state maps of P''_{rms} are given as a function of f_a/f_u for $\mathrm{Re}(h) = 2600$ and 3500 in Fig. 16, where each data point has been determined by calculating P''_{rms} over a 20-sec period. Note that this is not practical for real-time application, and so P''_{rms} is calculated using the last 0.1 sec of microphone data during real-time control. Upon inspection, the steady-state map is of the plateau type and will therefore require seeking a small nonzero slope. The maps for both Re have the same shape, and the optimal actuation input according to both maps is approximately $f_a/f_u = 2.4$ (the initiation of the plateau). This is in agreement with the contours of the suppression variable in Fig. 6.

The adaptive slope-seeking controller requires selection of the dither frequency (f_d), dither amplitude (a), slope reference (m), and integrator gain (k) for use in the control loop structure presented in Fig. 5 (see Sec. II E). These values were tuned experimentally, resulting in $f_d = 0.2$ Hz, $a = 2$, $m = -0.008$, and $k = -22$ and were selected to obtain quick and stable system performance without overshoot. Note that it is necessary for the dither frequency (0.2 Hz) to be slow in comparison to the vortex shedding frequency ($\geqslant$49.5 Hz) for the adaptive controller to function properly. The reader is directed to the work of Brackston *et al.* [61] for information regarding how these parameters affect the performance of the controller. The system response at $\mathrm{Re}(h) = 2600$ using the chosen parameters can be viewed in Fig. 17. The plot reveals large fluctuations in P''_{rms} prior to the controller being turned on. The periodic fluctuations in P''_{rms} occur at the frequency of the dither signal, and their large magnitude is indicative of the steep slope on the steady-state map. The controller acts to force these fluctuations to a small value once it is turned on. After approximately 30 sec, the controller settles at the optimal frequency $f_a/f_u = 2.4$ and maintains this value over time. This system response time (~30 sec) is long compared to the timescale of the unsteady wake dynamics (~0.02 sec). This is a consequence of using an adaptive slope-seeking controller, which requires such differences in timescales to operate properly [61]. Figure 17 reveals that there are still small oscillations in P''_{rms} at the dither frequency after reaching $f_a/f_u = 2.4$. This occurs because a small slope is used as the reference. If a slope of zero were to be sought, then the controller would

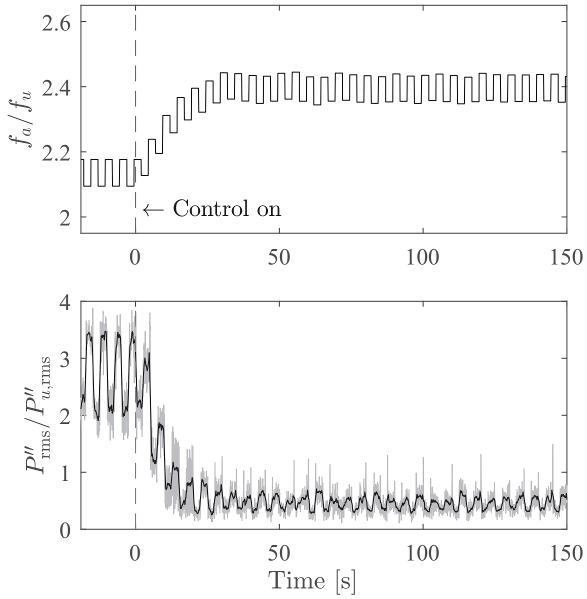

FIG. 17. System response of the adaptive slope-seeking controller at $\mathrm{Re}(h) = 2600$. The controller seeks the optimal input of $f_a/f_u = 2.4$ in approximately 30 sec and maintains this value over time. The values for P''_{rms} during control have been normalized by the rms of the filtered pressure fluctuations in the unforced wake ($P''_{u,\mathrm{rms}}$). In the lower plot, the gray line represents the true signal, and the black line is a moving average of the signal that has been added to better show the trend.

act to remove all oscillations in the signal because it is the oscillations that provide a measure of the slope.

The ability of the controller to respond to low-frequency disturbances has been investigated by changing the freestream velocity in the wind tunnel once the controller has settled at the optimal value. As can be seen in Fig. 18, the freestream disturbance was created by increasing, holding, then decreasing the wind tunnel velocity while staying within the Re range that the controller was designed for $[2600 \leqslant \mathrm{Re}(h) \leqslant 3500]$. The Strouhal number of the unsteady wake flow remains constant at $\mathrm{St}(h) = 0.20$ within this range, and so it has been used to determine f_u as the freestream velocity changes. This allows for monitoring f_a/f_u as long as the freestream velocity is known. The freestream velocity in the wind tunnel was recorded using a planar PIV measurement at an acquisition frequency of 25 Hz during the experiment. The results of the experiment are presented in Fig. 18. It can be seen that, after an adaptation period, the controller is able to reject the disturbance and reach the optimal actuation frequency of $f_a/f_u = 2.4$ at the new freestream velocity. The same is true when the Re is reduced back to its original value. However, the controller responds more quickly when the freestream velocity is increased as opposed to decreased. This is due to the fact that the current slope on the steady-state map determines the actuation frequency change using an integrator. The error in the slope is larger when the velocity is increased because the current position on the steady-state map of Fig. 16 is moved up the steep slope. When the velocity is decreased, the current position is moved further down the plateau. The difference between the reference m and the zero slope of the plateau does not offer as much of a driving force for the controller, and therefore the adaptation is slower. This also means that if the reference was set to zero for this particular plateau-style map, the controller would not be able to reject a reduction in the freestream velocity because the difference between the reference and the current slope would remain zero when the current position on the steady-state map was shifted up the plateau.

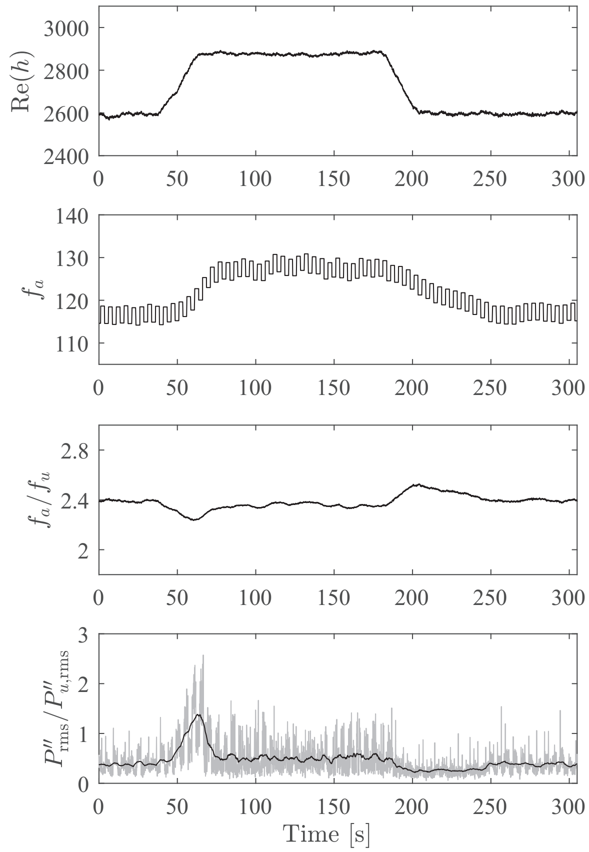

FIG. 18. System response to a simulated disturbance in the form of an unknown change in freestream velocity. The slope-seeking controller is able to reject the change in freestream velocity and eventually return to the optimal input of $f_a/f_u = 2.4$. The values for f_a/f_u were determined by using the mean of the square wave f_a. The gray line in the lower plot represents the true signal, and the black line is a moving average that has been added to better show the trend. P''_{rms} was normalized using the rms of the filtered pressure fluctuations in the unforced wake at $\mathrm{Re}(h) = 2600$.

IV. SUMMARY AND CONCLUSIONS

The manipulation of vortex shedding from a BTE using oscillating piezoelectric flaps with submillimeter displacement has been studied experimentally in a wind tunnel at $\mathrm{Re}(h) = 2600$. The actuators were operated to a maximum frequency of 180 Hz, and microphones installed at the trailing edge allowed for measuring the pressure fluctuations in the near-wake. The pressure measurements were used to investigate the impact of actuation over the entire operating range of the actuators for three different actuation methods: symmetric, asymmetric, and single actuation. The results indicated that all three methods were capable suppressing the dominant vortex shedding frequency in the wake at high actuation frequencies ($f_a > 2f_u$).

The pressure fluctuation results were used to select 18 actuation cases for detailed investigation using high-speed PIV. The selected cases covered all possible instances of vortex shedding amplification and suppression. POD was applied to the resulting vector fields to study the turbulent kinetic energy in the wake that is attributable to the primary vortex shedding instability. This value was 70% in the unforced wake, and it was obtained by summing the energy captured by the first two POD modes.

Asymmetric actuation at $f_a = f_u$ led to the maximum amplification of the wake. The energy captured by the first two POD modes increased to 90%, and the vortex shedding became more coherent and organized. The mean recirculation region in the wake shortened, suggesting a reduction in base pressure, and the turbulence intensities increased significantly. The time-resolved data revealed that amplification was caused by lock-in between the natural wake shedding and the actuation cycles, which enhanced vortex roll-up prior to their detachment from the BTE. The asymmetric flapping of the trailing edge was similar to a transversely oscillating cylinder, which can also lead to vortex shedding amplification [6,7]. Symmetric and single actuation were able to amplify vortex shedding to some degree, but their impact was less pronounced because one of the piezoelectric flaps was either turned off or working against the enhancement for these cases.

Maximum vortex shedding suppression occurred during symmetric and asymmetric actuation at $f_a = 3f_u$, which lead to the first two POD modes containing only 20% and 22% of the total fluctuation energy, respectively. Although symmetric actuation seems to slightly outperform asymmetric actuation, there did not seem to be a significant difference between their performances. Suppression resulted in a narrowed wake region and a longer formation length, suggesting a larger base pressure. The turbulence intensities in the wake were greatly reduced, and the dominant vortex shedding frequency was removed from the frequency spectrum of streamwise velocity fluctuation for at least $6h$ downstream. The time-resolved PIV data revealed that the mechanism of suppression was the generation of small spanwise vortices at the tips of the piezoelectric flaps at the frequency of actuation. The vortices acted to disrupt the communication between the separating shear layers, which lead to the complete suppression of vortex shedding. Fujisawa *et al.* [15] and Nati *et al.* [23] also reported vortex shedding suppression via shear-layer disruption, and Wiltse and Glezer [31] reported similar vortex formation when using piezoelectric flaps to manipulate an air jet. Single actuation at $f_a = 3.5f_u$ resulted in a large attenuation of the vortex shedding pattern but not its complete removal. Despite this, the results provide evidence that single actuation may result in complete suppression if actuation amplitudes or frequencies higher than what were investigated here were applied. This suggests that the disruption of a single shear layer may be sufficient for suppressing wake unsteadiness, provided that the disruption is large enough.

Symmetric actuation at $f_a = 1.5f_u$ acted to force both separating shear layers to roll into the wake simultaneously. Each actuation cycle formed one pair of symmetric, counter-rotating vortices in the near-wake, which quickly became unstable and shed to one side of the wake or the other in an alternating fashion before breaking into smaller vortices as they convected downstream. This process resulted in the vortex shedding frequency shifting to $0.75f_u$, as it requires two actuation cycles to produce a single shedding cycle in this case. Similar cases of forced near-wake symmetry have been reported by Nishihara *et al.* [66], Konstantinidis and Balabani [47], and Pastoor *et al.* [16] using different forms of actuation.

Finally, an adaptive slope-seeking controller was designed to suppress vortex shedding in real time. The controller acted to manipulate the frequency of symmetric actuation using the pressure fluctuation measurements at the BTE. Extensions to the standard extremum-seeking feedback loop that were proposed by Brackston *et al.* [61] were implemented here, resulting in a controller that was able to reach and maintain a near-optimal control input frequency within the designed operating range. The controller was capable of adapting to slow changes in freestream velocity.

ACKNOWLEDGMENTS

This work has been supported by the Natural Sciences and Engineering Research Council of Canada (Grant No. 2016-04646) and Future Energy Systems (Grant No. T14-P05). We would also like to thank Bernie Faulkner for manufacturing the blunt model, and Rick Conrad for developing the electronics necessary for operating the actuators and microphones.

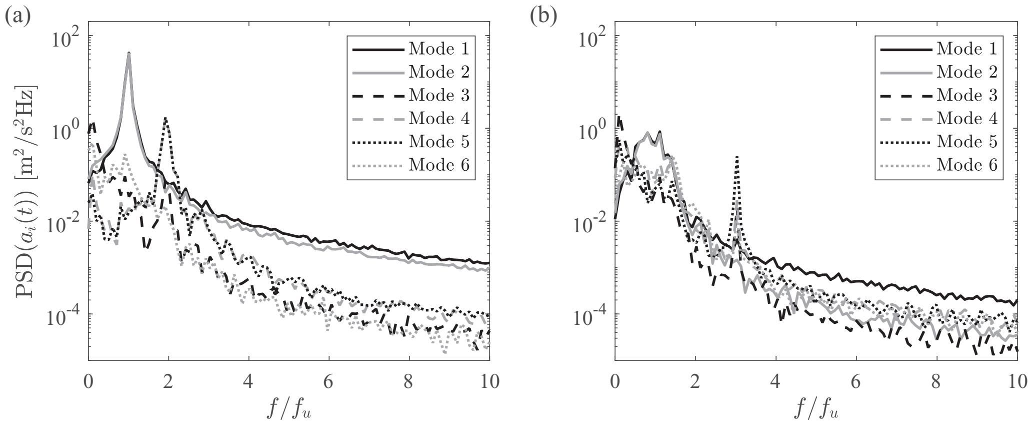

FIG. 19. Power spectral density (PSD) of the first six POD mode amplitudes $a_i(t)$ for (a) the unforced wake and (b) the wake suppressed by symmetric actuation at $f_a = 3f_u$.

APPENDIX: ORDER OF VORTEX SHEDDING DURING SUPPRESSION

A low-order representation of the unsteady wake is valid when the wake is dominated by vortex shedding [63]. However, it is not obvious whether this remains true when the unsteady wake is suppressed. The power spectral density (PSD) of the first six POD mode amplitudes $a_i(t)$ are plotted for the unforced and maximum suppression cases in Fig. 19 to show that the first two POD modes can be used to quantify the energy associated with vortex shedding during suppression. Figure 19(a) reveals that modes 1 and 2 for the unforced case feature large peaks in the spectrum at the unforced wake frequency f_u. Modes 3–5 have peaks at the first harmonic of f_u, but the peak heights are at least two orders of magnitude smaller than those of modes 1 and 2. Figure 19(b) shows similar behavior for modes 1 and 2 of the suppressed case, but the magnitude of the peaks are also two orders of magnitude smaller than those in the unforced wake case. Modes 3–6 in Fig. 19(b) show peaks at $3f_u$, which is the frequency of actuation. As mentioned in Sec. III D, suppression is caused by the cyclic formation of small spanwise vortices at the frequency of actuation, and these higher-order modes begin to capture those vortices. There is no evidence in Fig. 19(b) of the weakened vortex shedding pattern being captured by a higher-order POD construction. Its structure remains captured by modes 1 and 2. The higher-order modes (>6) each contain 3% or less of the energy and are therefore not dominant.

[1] H. Choi, W.-P. Jeon, and J. Kim, Control of flow over a bluff body, Annu. Rev. Fluid Mech. **40**, 113 (2008).
[2] C.-T. Chen, *Linear System Theory and Design* (Oxford University Press, Oxford, 1999).
[3] S. L. Brunton and B. R. Noack, Closed-loop turbulence control: Progress and challenges, Appl. Mech. Rev. **67**, 050801 (2015).
[4] L. N. Cattafesta III and M. Sheplak, Actuators for active flow control, Annu. Rev. Fluid Mech. **43**, 247 (2011).
[5] E. Berger, Suppression of vortex shedding and turbulence behind oscillating cylinders, Phys. Fluids **10**, S191 (1967).
[6] J. S. Tao, X. Y. Huang, and W. K. Chan, A flow visualization study on feedback control of vortex shedding from a circular cylinder, J. Fluids Struct. **10**, 965 (1996).

[7] H. M. Warui and N. Fujisawa, Feedback control of vortex shedding from a circular cylinder by cross-flow cylinder oscillations, Exp. Fluids **21**, 49 (1996).

[8] J. E. Ffowcs Williams and B. C. Zhao, The active control of vortex shedding, J. Fluids Struct. **3**, 115 (1989).

[9] K. Roussopoulos, Feedback control of vortex shedding at low Reynolds numbers, J. Fluid Mech. **248**, 267 (1993).

[10] X. Y. Huang, Feedback control of vortex shedding from a circular cylinder, Exp. Fluids **20**, 218 (1996).

[11] N. Fujisawa and T. Nakabayashi, Neural network control of vortex shedding from a circular cylinder using rotational feedback oscillations, J. Fluids Struct. **16**, 113 (2002).

[12] J.-C. Lin, J. Towfighi, and D. Rockwell, Near-wake of a circular cylinder: Control by steady and unsteady surface injection, J. Fluid Struct. **9**, 659 (1995).

[13] X.-D. Shi and L.-H. Feng, Control of flow around a circular cylinder by bleed near the separation points, Exp. Fluids **56**, 214 (2015).

[14] D. R. Williams, H. Mansy, and C. Amato, The response and symmetry properties of a cylinder wake subjected to localized surface excitation, J. Fluid Mech. **234**, 71 (1992).

[15] N. Fujisawa, G. Takeda, and N. Ike, Phase-averaged characteristics of flow around a circular cylinder under acoustic excitation control, J. Fluid Struct. **19**, 159 (2004).

[16] M. Pastoor, L. Henning, B. R. Noack, R. King, and G. Tadmor, Feedback shear layer control for bluff body drag reduction, J. Fluid Mech. **608**, 161 (2008).

[17] L. H. Feng and J. J. Wang, Circular cylinder vortex-synchronization control with a synthetic jet positioned at the rear stagnation point, J. Fluid Mech. **662**, 232 (2010).

[18] Y. Qu, J. Wang, M. Sun, L. Feng, C. Pan, Q. Gao, and G. He, Wake vortex evolution of a square cylinder with a slot synthetic jet positioned at the rear surface, J. Fluid Mech. **812**, 940 (2017).

[19] G. Artana, R. Sosa, E. Moreau, and G. Touchard, Control of the near-wake flow around a circular cylinder with electrohydrodynamic actuators, Exp. Fluids **35**, 580 (2003).

[20] T. N. Jukes and K.-S. Choi, Control of unsteady flow separation over a circular cylinder using dielectric-barrier-discharge surface plasma, Phys. Fluids **21**, 094106 (2009).

[21] A. V. Kozlov and F. O. Thomas, Bluff-body flow control via two types of dielectric barrier discharge plasma actuation, AIAA J. **49**, 1919 (2011).

[22] N. Benard and E. Moreau, Response of a circular cylinder wake to a symmetric actuation by non-thermal plasma discharges, Exp. Fluids **54**, 1467 (2013).

[23] G. Nati, M. Kotsonis, S. Ghaemi, and F. Scarano, Control of vortex shedding from a blunt trailing edge using plasma actuators, Exp. Therm. Fluid Sci. **46**, 199 (2013).

[24] S. Bhattacharya and J. W. Gregory, Effect of three-dimensional plasma actuation on the wake of a circular cylinder, AIAA J. **53**, 958 (2015).

[25] A. Naghib-Lahouti, H. Hangan, and P. Lavoie, Distributed forcing flow control in the wake of a blunt trailing edge profiled body using plasma actuators, Phys. Fluids **27**, 035110 (2015).

[26] I. Korkischko and J. R. Meneghini, Suppression of vortex-induced vibration using moving surface boundary-layer control, J. Fluids Struct. **34**, 259 (2012).

[27] J. C. Schulmeister, J. M. Dahl, G. D. Weymouth, and M. S. Triantafyllou, Flow control with rotating cylinders, J. Fluid Mech. **825**, 743 (2017).

[28] L. N. Cattafesta III, S. Garg, and D. Shukla, Development of piezoelectric actuators for active flow control, AIAA J. **39**, 1562 (2001).

[29] J. Mathew, Q. Song, B. V. Sankar, M. Sheplak, and L. N. Cattafesta III, Optimized design of piezoelectric flap actuators for active flow control, AIAA J. **44**, 2919 (2006).

[30] M. bin Mansoor, N. Reuther, S. Köble, M. Gérard, H. Steger, P. Woias, and F. Goldschmidtböing, Parametric modeling and experimental characterization of a nonlinear resonant piezoelectric actuator designed for turbulence manipulation, Sens. Actuators A: Phys. **258**, 14 (2017).

[31] J. M. Wiltse and A. Glezer, Manipulation of free shear flows using piezoelectric actuators, J. Fluid Mech. **249**, 261 (1993).

[32] J. M. Wiltse and A. Glezer, Direct excitation of small-scale motions in free shear flows, Phys. Fluids **10**, 2026 (1998).

[33] S. A. Jacobson and W. C. Reynolds, Active control of streamwise vortices and streaks in boundary layers, J. Fluid Mech. **360**, 179 (1998).

[34] W.-P. Jeon and R. F. Blackwelder, Perturbations in the wall region using flush mounted piezoceramic actuators, Exp. Fluids **28**, 485 (2000).

[35] D.-H. Kim, J.-W. Chang, and J.-S. Cho, Flow disturbances depending on excitation frequency on a flat plate by a piezoceramic actuator, J. Vis. **16**, 111 (2013).

[36] H. L. Bai, Y. Zhou, W. G. Zhang, S. J. Xu, Y. Wang, and R. A. Antonia, Active control of a turbulent boundary layer based on local surface perturbation, J. Fluid Mech. **750**, 316 (2014).

[37] L. N. Cattafesta III, Q. Song, D. R. Williams, C. W. Rowley, and F. S. Alvi, Active control of flow-induced cavity oscillations, Prog. Aerosp. Sci. **44**, 479 (2008).

[38] M. Amir and K. Kontis, Application of piezoelectric actuators at subsonic speeds, J. Aircraft **45**, 1419 (2008).

[39] O. Bilgen, C. de Marqui Junior, K. B. Kochersberger, and D. J. Inman, Piezoceramic composite actuators for flow control in low Reynolds number airflow, J. Intell. Material Syst. Struct. **21**, 1201 (2010).

[40] M. M. Zhang, L. Cheng, and Y. Zhou, Closed-loop-controlled vortex shedding and vibration of a flexibly supported square cylinder under different schemes, Phys. Fluids **16**, 1439 (2004).

[41] M. M. Zhang, Y. Zhou, and L. Cheng, Closed-loop-manipulated wake of a stationary square cylinder, Exp. Fluids **39**, 75 (2005).

[42] C. H. K. Williamson and R. Govardhan, Vortex-induced vibrations, Annu. Rev. Fluid Mech. **36**, 413 (2004).

[43] A. Ongoren and D. Rockwell, Flow structure from an oscillating cylinder Part 2. Mode competition in the near wake, J. Fluid Mech. **191**, 225 (1988).

[44] S. J. Xu, Y. Zhou, and M. H. Wang, A symmetric binary-vortex street behind a longitudinally oscillating cylinder, J. Fluid Mech. **556**, 27 (2006).

[45] E. Detemple-Laake and H. Eckelmann, Phenomenology of Kármán vortex streets in oscillatory flow, Exp. Fluids **7**, 217 (1989).

[46] C. Barbi, D. P. Favier, C. A. Maresca, and D. P. Telionis, Vortex shedding lock-on of a circular cylinder in oscillatory flow, J. Fluid Mech. **170**, 527 (1986).

[47] E. Konstantinidis and S. Balabani, Symmetric vortex shedding in the near wake of a circular cylinder due to streamwise perturbations, J. Fluids Struct. **23**, 1047 (2007).

[48] B. Gibeau, C. R. Koch, and S. Ghaemi, Secondary instabilities in the wake of an elongated two-dimensional body with a blunt trailing edge, J. Fluid Mech. **846**, 578 (2018).

[49] M. R. Johnson and L. W. Kostiuk, Efficiencies of low-momentum jet diffusion flames in crosswinds, Combust. Flame **123**, 189 (2000).

[50] A. Roshko, On the development of turbulent wakes from vortex streets, NACA report 1191 (1954).

[51] M. S. Petrusma and S. L. Gai, Bluff body wakes with free, fixed, and discontinuous separation at low Reynolds numbers and low aspect ratio, Exp. Fluids **20**, 189 (1996).

[52] K. B. Ariyur and M. Krstić, *Real-Time Optimization by Extremum-Seeking Control* (Wiley, New York, 2003).

[53] J. F. Beaudoin, O. Cadot, J. L. Aider, and J. E. Wesfreid, Bluff-body drag reduction by extremum-seeking control, J. Fluids Struct. **22**, 973 (2006).

[54] J. F. Beaudoin, O. Cadot, J. L. Aider, and J. E. Wesfreid, Drag reduction of a bluff body using adaptive control methods, Phys. Fluids **18**, 085107 (2006).

[55] R. Becker, R. King, R. Petz, and W. Nitsche, Adaptive closed-loop separation control on a high-lift configuration using extremum seeking, AIAA J. **45**, 1382 (2007).

[56] N. Benard, E. Moreau, J. Griffin, and L. N. Cattafesta III, Slope seeking for autonomous lift improvement by plasma surface discharge, Exp. Fluids **48**, 791 (2010).

[57] T. Chabert, J. Dandois, and E. Garnier, Experimental closed-loop control of flow separation over a plain flap using slope seeking, Exp. Fluids **55**, 1797 (2014).

[58] T. Chabert, J. Dandois, and E. Garnier, Experimental closed-loop control of separated-flow over a plain flap using extremum seeking, Exp. Fluids **57**, 37 (2016).

[59] K. Kim, C. Kasnakoğlu, A. Serrani, and M. Samimy, Extremum-seeking control of subsonic cavity flow, AIAA J. **47**, 195 (2009).

[60] A. Wu, Y. Zhou, H. L. Cao, and W. J. Li, Closed-loop enhancement of jet mixing with extremum-seeking and physics-based strategies, Exp. Fluids **57**, 107 (2016).

[61] R. D. Brackston, A. Wynn, and J. F. Morrison, Extremum seeking to control the amplitude and frequency of a pulsed jet for bluff body drag reduction, Exp. Fluids **57**, 159 (2016).

[62] L. Sirovich, Turbulence and the dynamics of coherent structures, parts I–III, Q. Appl. Math. **45**, 561 (1987).

[63] B. W. van Oudheusden, F. Scarano, N. P. van Hinsberg, and D. W. Watt, Phase-resolved characterization of vortex shedding in the near wake of a square-section cylinder at incidence, Exp. Fluids **39**, 86 (2005).

[64] C. H. K. Williamson, Vortex dynamics in the cylinder wake, Annu. Rev. Fluid Mech. **28**, 477 (1996).

[65] See Supplemental Material at http://link.aps.org/supplemental/10.1103/PhysRevFluids.4.054704 for movies of the unforced wake, vortex shedding amplification, vortex shedding suppression, and forced near-wake symmetry.

[66] T. Nishihara, S. Kaneko, and T. Watanabe, Characteristics of fluid dynamic forces acting on a circular cylinder oscillated in the streamwise direction and its wake patterns, J. Fluids Struct. **20**, 505 (2005).